Ultrafast dynamics of single-pulse femtosecond laser-induced periodic ripples on the surface of a gold film

Ke Cheng,[1] Jukun Liu,[1,2] Kaiqiang Cao,[1] Long Chen,[1] Yuchan Zhang,[1] Qilin Jiang,[1]
Donghai Feng,[1] Shian Zhang,[1] Zhenrong Sun,[1] and Tianqing Jia[1,*]

[1]*State Key Laboratory of Precision Spectroscopy, College of Physics and Materials Science,*
East China Normal University, Shanghai 200062, People's Republic of China
[2]*College of Science, Shanghai Institute of Technology, Shanghai 201418, People's Republic of China*

The ultrafast dynamics of periodic ripples are studied during their formation on the surface of a gold film with a prefabricated nanogroove. These transient ripples are induced by a single 800-nm, 50-fs laser pulse and are observed by a collinear pump-probe imaging method. When the laser polarization is parallel to the nanogroove, transient ripples begin appearing after an elapsed time of 25–80 ps, and become clear and regular at 400–600 ps. The ripple period increases from 685 to 770 nm as the laser fluence F increases from 0.73 to 3.42 J/cm^2. The evolution of temperature and lattice temperature are theoretically studied using the two-temperature model. When the laser fluence F is above 0.73 J/cm^2, the electron temperature rises to several 10^4 K, and the collision frequency rises above 10^{16}/s, which further causes the localization of hot electrons. Moreover, the d-band electrons can be excited through two-photon absorption and become free electrons. Using the dielectric constant of the excited states, which includes the effects of hot-electron localization and d-band transitions, the period predicted by the surface-plasmon-polarization (SPP) model accords well with experimental results. Both theory and experiment give support to SPP excitations playing a prominent role in the formation of periodic ripples induced by femtosecond laser pulses.

I. INTRODUCTION

Laser-induced periodic surface structures were discovered by Birnbaum in 1965 on a semiconductor surface irradiated with a ruby laser [1]. Since then, such nanostructures have been studied on different material surfaces [2–11]. The laser-induced nanostructures change surface characteristics, which gives rise to many applications such as broadband absorption [12–14], enhanced photoluminescence [15–17], surface coloring [18,19], and wettability [20–22]. Controlling size and shape plays a role in achieving a desired functionality. Studying the mechanism underpinning their formation is helpful in controlling such nanostructures.

Over the past half century [1–11,23], several models have been proposed to explain the formation mechanism. The "surface scattered wave" model attributes the formation of ripples to an interference between the incident light field and the surface-scattered light [2,11,23]. The "self-organization" model ascribes the formation to surface instabilities in the melt layer [24–26]. The "surface-plasmon-polarization (SPP)" model describes the formation as originating from SPP excitations, which generate a spatially modulated light field and energy deposition that forms the ripples [10,27,28]. Other models such as the Sipe diffraction theory [3] and Coulomb explosion [29] have also been developed to explain the ripple formation. The underlying mechanism of laser-induced ripples, however, continues to be an active topic.

The SPP model has been widely studied and explains well the formation of periodic ripples on semiconductors induced by femtosecond laser pulses [30–32]. Experiments show that the ripple period increases with laser fluence, as described by the SPP model; the higher the laser fluence, the higher is the electron density on the excited surface. Given the relationship between dielectric constant and electron number density, the period calculated by the SPP model increases with laser fluence, in a manner consistent with the experimental results. However, the SPP model cannot account for the period dependence of ripples formed on metal surfaces [11,33,34]. Using the dielectric constants of the ground states of gold, copper, and aluminum, the SPP wavelengths are much larger than that of the ripples [7,28,35,36]. The d-band electrons in copper and silver can be excited into states above the Fermi surface [37,38]. The free-electron density and plasma frequency both increase with laser fluence, giving longer SPP wavelengths. The widely studied SPPs of silver and gold nanostructures are very strong. However, the periods differ significantly from the SPP model, thus posing a conundrum.

Surface ripples are usually induced under multiple laser pulses. After each laser pulse, material is ablated and surface defects form. Therefore, not only is there an uncertainty in the formation mechanism but the orientation of ripples is complex [32,33]. Distinguishing, for example, the effects of scattered light and grating coupling feedback on the formation of periodic ripples is difficult. Recently, results using a single femtosecond laser pulse [32,39–41] provided fundamental information on the laser-matter interaction aimed at investigating the origin of the ripples.

*tqjia@phy.ecnu.edu.cn

Noncollinear [42,43] and collinear pump-probe imaging techniques [28,32,44] were applied to observe ripple formation to gain further understanding of its mechanism. Murphy and co-workers reported the ripple formation irradiated by multiple pulses by noncollinear pump-probe imaging [42]. By using optical diffraction microscopy, Kafka *et al.* detected the formation of ripples on Cu film irradiated by a single femtosecond pulse [43]. By this imaging technique, the ripples were observed only on the periphery of the irradiated area. Using a collinear pump-probe imaging technique, Jia and Zhou studied the ripple formation on the whole ablation area irradiated by multiple pulses [28,44]. Recently, Liu *et al.* reported on the ultrafast imaging of the formation of periodic ripples on a Si surface with a prefabricated nanogroove induced by a single femtosecond laser pulse [32].

The formation of periodic ripples is related to phase transformations such as melting and vaporization. The two-temperature model (TTM) was widely used to calculate the evolution of both the electron and lattice temperatures under femtosecond laser pulses [34,45]. Wang and Guo performed a TTM-based study of the ripples on noble-metal surfaces, and found that the electron–phonon coupling strength played a dominant role in the formation processes [45]. Liu *et al.* reported the ultrafast dynamics of laser-matter interaction, such as free carrier excitation, carrier and lattice heating, and SPP excitation by TTM, which explained well the time of emergence and ripple periods on a Si surface radiated by a femtosecond laser with different fluences [34].

In this paper, from experiments and from theory, we analyze the ultrafast dynamics involved in ripple formation on the surface of gold films induced by a single 800-nm, 50-fs laser pulse. When the laser polarization is parallel to the nanogroove, transient ripples begin to appear after an elapsed time of 25–80 ps, and become regular and distinct after 400–600 ps. Their period increases from 685 to 770 nm as laser fluence increases from 0.73 to 3.42 J/cm^2. The evolution of the electron and lattice temperatures were studied using the TTM. We propose that when the collision frequency of hot electrons rises above the 800-nm laser frequency, these hot electrons are unable to oscillate synchronously with the laser field and become localized. Moreover, the d-band electrons can be excited through two-photon absorption into the conduction band. With a dielectric constant for excited states that includes the effects of hot-electron localization and d-band transitions, the ripple period predicted by the SPP model accords well with that from experiments.

II. EXPERIMENT SETUP AND SAMPLE

A. Experimental setup

The experimental setup for the pump-probe imaging [Fig. 1(a)] is similar to that presented in [44]. The laser system used is a commercial Ti:sapphire regenerative amplifier laser (Legend Elite, Coherent), which produces 800-nm, 50-fs, 3.5-mJ laser pulses with a repetition rate of 1–1000 Hz. Single laser pulses are generated using a mechanical shutter. The laser beam is split into a pump beam and a probe beam using a 50:50 beam splitter. The pump beam is used to induce the surface structures on gold film. The probe beam goes
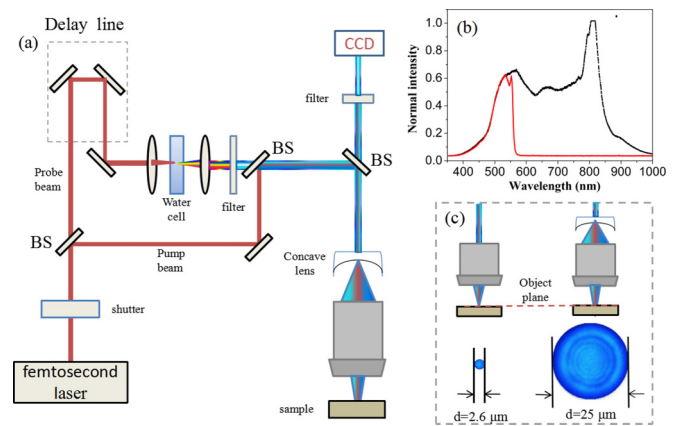

FIG. 1. (a) Experiment setup of the pump-probe imaging system; (b) Spectra of the white-light pulse with (red solid curve) and without (black dotted curve) the short-wave-pass filter; (c) Laser-beam intensity on the object plane with and without the concave lens.

through a delay line with a resolution of 1 μm. The probe pulse is focused onto a 10-mm-thick water cell to generate a white-light pulse with a spectrum in the range of 450–900 nm [Fig. 1(b)]. The optical spectrum is narrowed to a range of 450–570 nm after going through a short-wave-pass filter with a cutoff wavelength of 550 nm.

The pump and probe pulses are combined by a beam splitter and then inputted collinearly to a microscope (80i, Nikon Instruments, Inc.), in which an objective lens [100×, numerical aperture (NA) = 0.9] is used to focus the pump pulse onto the gold surface. The white light is reflected from the sample, travels through a short-wave-pass filter with a cutoff wavelength of 600 nm, and is registered by a charge-coupled device (CCD) camera. The filter is used to block the scattered light from the pump pulse.

To obtain distinct images of the surface structures, the sample is placed in the object plane, close to the focus plane. The laser focus is only 2.6 μm in diameter, which is too small to obtain enough ripples. Therefore, a concave lens with $f = -150$ mm is placed in front of the objective lens to disperse the pump pulse and expand the laser focus to 25 μm in diameter with several diffraction rings appearing due to the concave lens [Fig. 1(c)]. The intensity distribution of the laser field at the object plane is registered by a CCD camera using the blue light emitted from a ZnSe crystal surface. The laser pulse energy E_P on the sample is measured by an energy sensor (PE9-C, Ophir), and the laser fluence is then calculated from $F = E_P/S$, where S is the area of laser focus at the object plane.

The optical spectrum of the white-light pulse is a significant parameter because it determines the spatial and temporal resolution in the experiments. The spectrum after short-wave-pass filtering covers the wavelength range 450–570 nm, corresponding to a spatial resolution of 345 nm. The duration of the white-light pulse is estimated to be 0.6 ps at the sample surface [32].

B. Sample

The 200-nm-thick gold film is deposited by magnetron sputtering on a 25-mm-diameter glass substrate. A
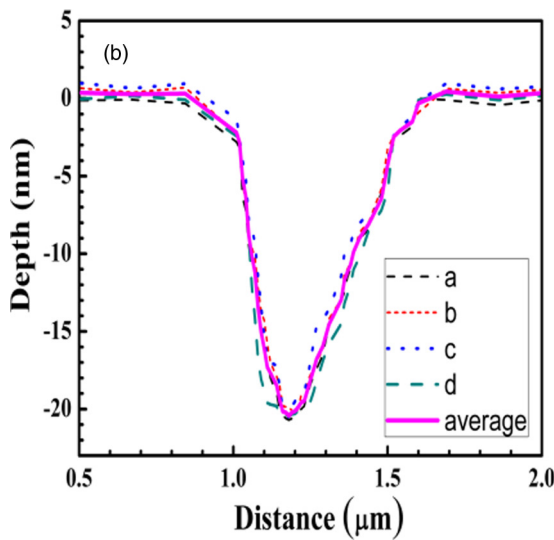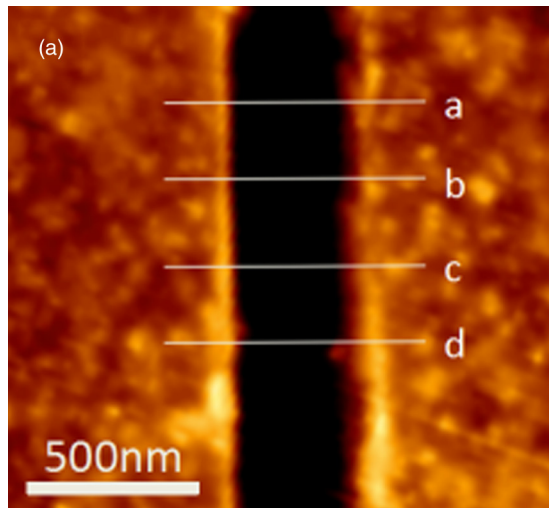
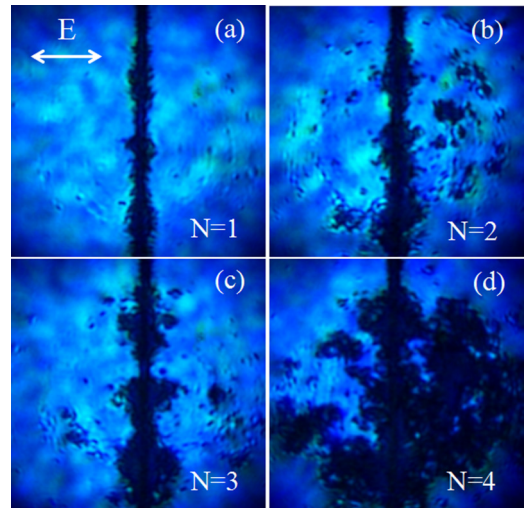FIG. 2. Prefabricated nanogroove: (a) Atomic force microscope (AFM) image; (b) Cross sections at different positions marked in (a).

FIG. 3. Optical micrographs of laser-induced surface microstructures after irradiation by one to four laser pulses at a fluence of $1.0\,\mathrm{J/cm^2}$. The horizontal double arrow in (a) indicates the direction of laser polarization.

nanogroove is etched onto the film using laser direct writing. The 800-nm, 50-fs, 1-kHz laser beam is focused by a water immersion lens ($100\times$, NA = 1.2). The 450-nm-wide uniform nanogroove is fabricated under a laser fluence of $F = 0.8\,\mathrm{J/cm^2}$ and scanning velocity of 50 μm/s (Fig. 2). The depth of the groove varies between 18 and 22 nm with an average depth of 20 nm. After fabricating the groove, the sample is cleansed with acetone and de-ionized water. The gold wafer is mounted on a three-axis translation stage with an accuracy of 1 μm. After laser ablation, the sample is moved to present a pristine area for further experimentation.

III. EXPERIMENTAL RESULTS AND DISCUSSION

A. Evolution of surface microstructures after irradiation by one to four laser pulses

Following ablation and after the molten layer has solidified, images were taken of the surface microstructures (Fig. 3) irradiated by one to four pump pulses at a fluence of $1.0\,\mathrm{J/cm^2}$ [28]. After the first pulse, several tiny curved streaks appear

on the sample surface [Fig. 3(a)]. With a second pulse, some short shallow ripples appear; however, measuring its period is difficult. Following three pulses, the initially formed short ripples do not grow deeper or more regular. There are several dark spots and random microstructures in the center of the ablated area [46]. After four pulses, the sample surface is badly damaged. Following each laser pulse treatment at different fluences, the sample surface is also scrutinized but no regular ripples are observed [28].

B. Ultrafast dynamics during a single-pulse ablation

The formation of periodic ripples is usually observed under a scanning electron microscope [47,48] or atomic force microscope [49]. However, the transient processes during laser ablation cannot be investigated in this way. Although no ripples were observed in the ablation area on the gold film, this does not mean that they never formed. Therefore, to investigate the ultrafast dynamics of ripple formation, we performed collinear pump-probe imaging over elapsed times ranging from -5 ps to 75 ns.

The sample surface was irradiated with a single laser pulse at a fluence of $1.96\,\mathrm{J/cm^2}$, which is much larger than the ablation threshold of $0.5\,\mathrm{J/cm^2}$ [50]. The laser polarization is perpendicular to the direction of the prefabricated nanogroove. Before the arrival of the pump pulse, only the nanogroove is observed [Fig. 4(a)]. Three characteristic features are identifiable: (1) No distinct change on the gold film is seen from 0 to 30 ps, in agreement with previous experimental phenomena [28]; (2) rudimentary ripples emerge at 45 ± 10 ps, becoming more numerous and distinct as time elapses; and (3) between 400 and 600 ps, the ripples appear most distinct and regular, as found in the results on a Cu substrate [43]. The ripples are perpendicular to the laser polarization with a period of 740 ± 10 nm.

The intensity curves at the elapsed times 30, 50, 90, 200, 400, and 600 ps (Fig. 5) are normalized and manually offset
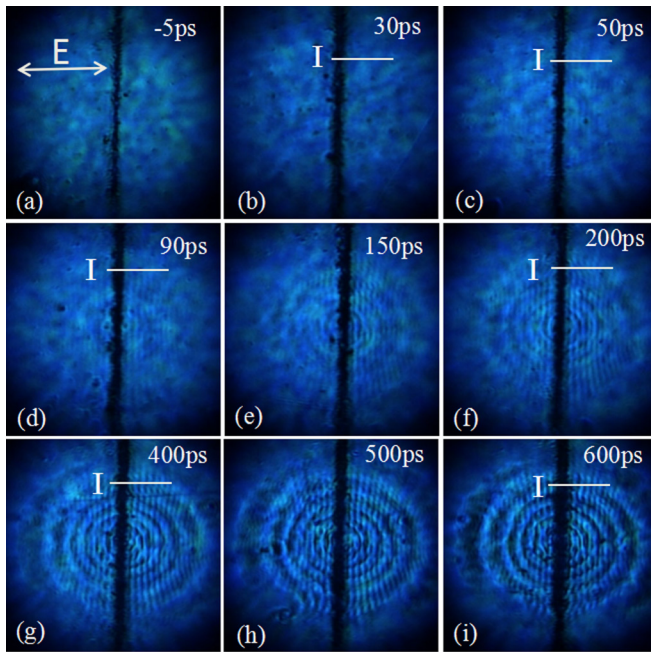
FIG. 4. Optical images measured at different elapsed times. The horizontal double arrow indicates the direction of laser polarization. The lines labeled by "I" mark the same position.

for convenient comparison. The contrast ratios become larger with increasing elapsed time. The two marked lines show that the positions of the crests and valleys remain stationary as the ripples intensify from the periodic distribution of the deposited laser energy [44].

The disappearance of the periodic ripples along with the solidification of the ablation spot was imaged (Fig. 6). At an elapsed time of 0.8 ns, the ripples begin to blur slightly because the probe light is being absorbed and scattered by ablated material. After 2 ns, the ripples become very fuzzy because of strong thermal effects and ejections. After 4 ns,
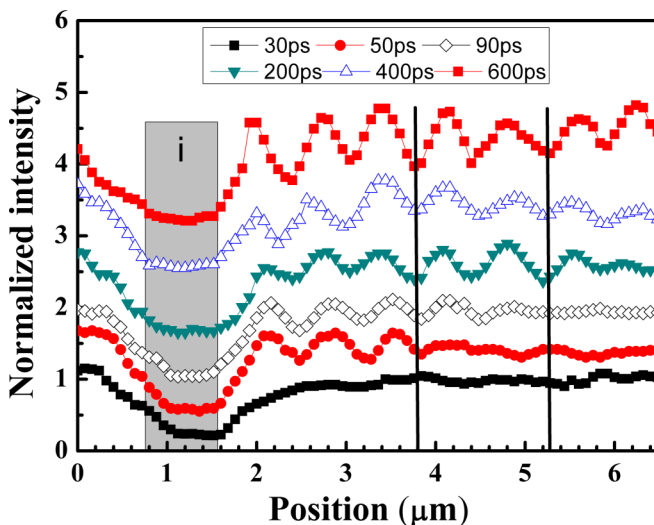

FIG. 5. Normalized intensity of the CCD pixels along the lines "I" of Fig. 4. The "i" rectangle outlines the nanogroove region.
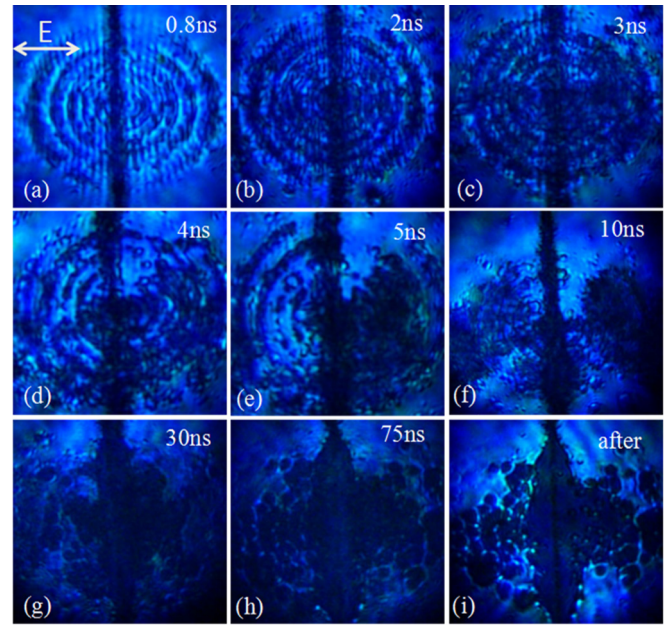

FIG. 6. Optical images showing the disappearance of the ripples and the solidification of the ablation spot.

a large thin layer of the surface has melted, and the ripples disappear entirely except for a few short fuzzy ripples at the edge of the ablated area. After 5 ns, only a few striped arcs appear on the surface arising from diffraction effects from the concave lens [28]. These striped arcs also disappear at 10 ns due to strong melting, hydrodynamic effects, and ablation. The surface begins to form many microfragments. After an ablation lasting 75 ns, the surface structures appear very similar to those in Fig. 6(i), indicating that the ablative ejection has nearly finished, and cooling and solidification subsequently take hold.

C. Ultrafast dynamics of the formation of periodic ripples induced by a single pulse with different fluences

Many studies have reported on the effect of femtosecond laser fluence and pulse number on ripple formation [11,48,51]. When the number of pulses is the same, ripple period increases with laser fluence but decreases with increases in pulse number at constant laser fluence. In the last section, we studied the ultrafast dynamics of the formation of periodic ripples induced by a single pulse with $F = 1.96 \, \text{J/cm}^2$. In the following, we analyze ripple formation induced by single pulses of different fluences.

The evolution of ripple formation under these circumstances is shown in Figs. 7 and 8. To clearly show the ripples, only the central part of each ablation spot is presented. For a fluence of $0.73 \, \text{J/cm}^2$, very fuzzy ripples appear at an elapsed time of 100 ± 30 ps. For a higher fluence of $1.0 \, \text{J/cm}^2$, ripples begin to appear at an elapsed time of 65 ± 20 ps. For low fluences, there are no clear and regular ripples observed [Figs. 7(e)–7(h)]. For a fluence of $1.47 \, \text{J/cm}^2$, fuzzy ripples appear at 50 ± 15 ps. Similar with the case of $F = 1.96 \, \text{J/cm}^2$, very regular and clear ripples form on the sample surface during the interval 400–600 ps.
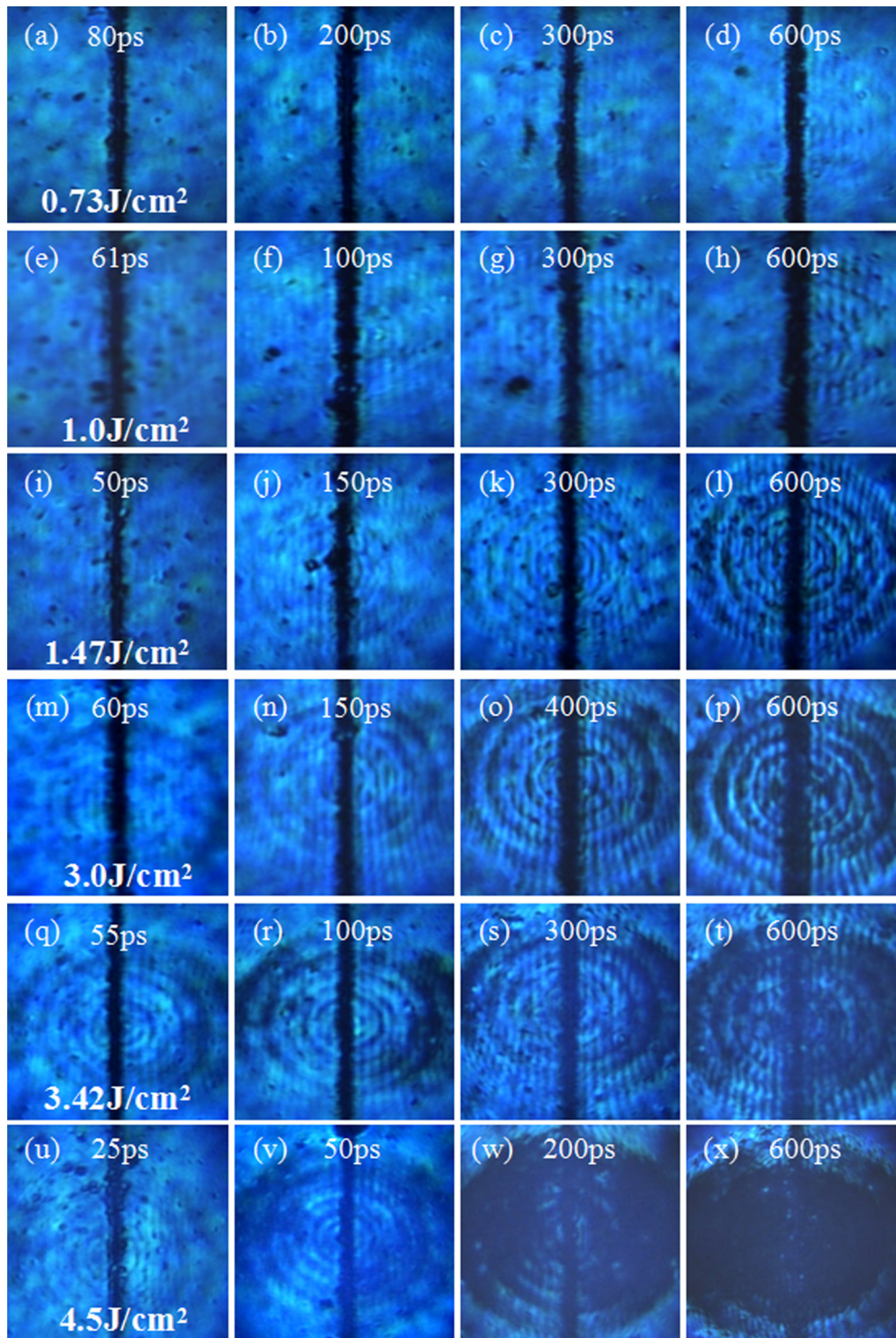
FIG. 7. Evolution of ripple formation for laser fluence of 0.73, 1.0, 1.47, 3.0, 3.42, and 4.5 J/cm^2. The gain coefficient of the CCD camera is adjusted to obtain suitably bright pictures in each row.

With the fluence increased to 3.0 J/cm^2, ripples emerged at 60 ± 20 ps. Compared with the emergence time for $F = 1.96$ J/cm^2, the ripples appear later. Two competing factors in laser fluence affect the observation of ripples. Electron and lattice temperatures rise more rapidly and higher for larger laser fluences [32,52,53], causing ripples to be observed earlier, as seen for $F = 0.73-1.96$ J/cm^2. Nevertheless, large amounts of ablated material fly out from the sample surface,

absorb and scatter the probe light [54,55], causing images to become fuzzy. The ripples initially formed are very shallow and are very easily overwhelmed, leading to longer elapsed times being observed [Figs. 7(m)–7(p)].

The situation for $F = 4.5$ J/cm^2 is much different from that with F in the range $1.47-3.42$ J/cm^2. The ripples begin to appear very early, at an elapsed time of 25 ± 5 ps. This is because a high-fluence pulse heats the electrons and lattice
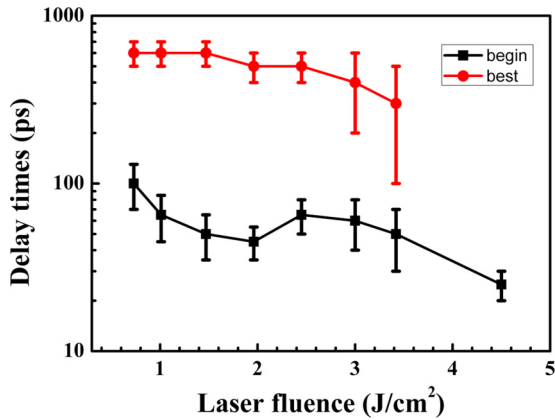
FIG. 8. Elapsed times when ripples emerge and are the most regular and clearest.

FIG. 10. Optical images of the ablation spot observed at different elapsed times. The horizontal double arrow indicates the direction of laser polarization.

rapidly to very high temperatures, initiating strong ionization and ablation [54,55]. The ejected plume, including dense plasma and tiny droplets, absorb and scatter the probe light considerably. Therefore, the images at 200 and 600 ps are too dark to observe the ripples and other surface microstructures clearly [Figs. 7(u)–7(x)].

Figure 9 shows that ripple period increases from 685 ± 10 nm to 770 ± 10 nm when fluence increases from 0.73 to $3.42 \, \text{J/cm}^2$, which is similar to the results on the surfaces of Si, GaP, and ZnO crystals [30–32]. It was believed that the number density of the excited electrons increases with laser fluence, leading to longer SPP wavelengths and larger periods. For metal surfaces, periods also increased with laser fluences, caused by the interaction of laser field with the laser-produced surface plasma [11,34].

The SPP model does not explain well the ripple period of gold surfaces. The SPP wavelength excited by 800-nm light is 780 nm, which is obviously greater than the experimental results (Fig. 9). The higher the laser fluence, the higher the free-electron density produced by the laser itself, which induces longer SPP wavelengths and ripple period. These results deviate significantly from the experimental values. Explaining the experimental phenomenon from theory is the focus of the next section.
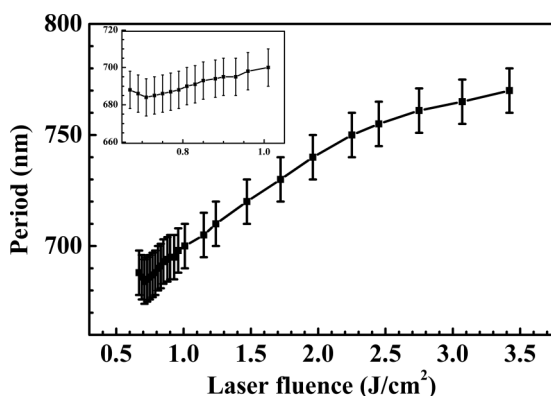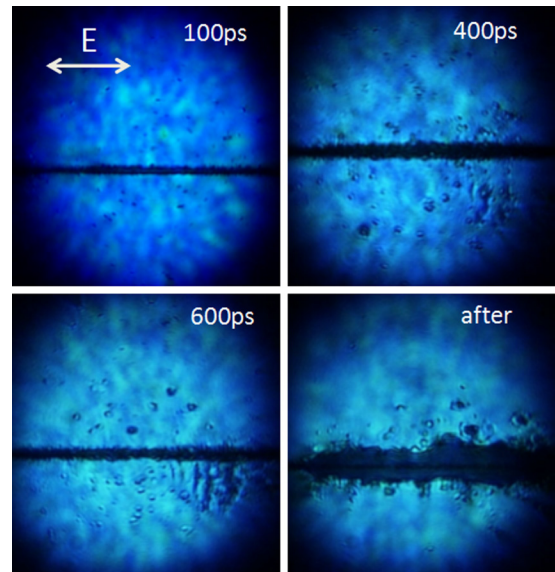
D. Polarization effect

Laser polarization significantly affects the SPP excitations [32,39]. To check further if the SPP excitation plays an important role in the ripple formations, we rotated the nanogroove by 90° so that the laser polarization direction is parallel to the nanogroove. Figure 10 shows the time-resolved images of surface microstructures at different elapsed times after irradiation by the pulse at a fluence of $1.56 \, \text{J/cm}^2$. Different from all previous results, no periodic ripples were observed during the entire duration of laser ablation. When the laser polarization direction is parallel to the nanogroove, SPP cannot be efficiently excited, which indicates that SPP excitation plays a key role in ripple formation.

IV. THEORY

A. Dielectric constant in the ground state

In the ground state, the dielectric constant of gold consists of two parts. One is the excitation of free electrons based on the Drude model, and the other is the interband transition based on the Lorentz resonance model. The dielectric constant is described by a modified version of the Drude-Lorentz model [56],

$$\varepsilon(\omega) = 1 - \frac{f_0 \omega_p^2}{\omega(\omega - i\Gamma_0)} + \sum_{j=1}^{3} \frac{f_j \omega_p^2}{\omega_j^2 - \omega^2 + i\omega\Gamma_j}, \quad (1)$$

where ω is the laser frequency (i.e., $\omega = 3.75 \times 10^{14}$ Hz for an 800-nm laser), $\sqrt{f_0}\omega_p$ the plasma frequency associated with the oscillator strength $f_0 = 0.76$, and the damping constant $\Gamma_0 = 1.28 \times 10^{13}$ Hz at room temperature. In regard to the interband transitions, there are three excitations with frequencies ω_j, strengths f_j, and lifetime $1/\Gamma_j$ ($j = 1, 2, 3$). The values of these parameters are listed in Table I. The dielectric constant simulated with Eq. (1) and the parameters

FIG. 9. Dependence of ripple period on laser fluence.

TABLE I. Parameters for the Drude-Lorentz model.

Symbol	Value	Symbol	Value	Symbol	Value
$\hbar\omega_p$ (eV)	9.03	$\hbar\Gamma_0$ (eV)	0.053	f_0	0.76
$\hbar\omega_1$ (eV)	0.415	$\hbar\Gamma_1$ (eV)	0.241	f_1	0.043
$\hbar\omega_2$ (eV)	0.830	$\hbar\Gamma_2$ (eV)	0.345	f_2	0.005
$\hbar\omega_3$ (eV)	2.969	$\hbar\Gamma_3$ (eV)	0.870	f_3	0.233

in Table I agree well with the experimental data for photon energies in the range 0.7–1.9 eV [57,58], and is used in the theoretical calculation in Fig. 11.

B. Surface plasmon polarization and periodic ripples

Periodic ripples on semiconductor and metal surfaces induced by femtosecond laser pulses are attributed to laser-induced SPPs [9,27,59]. The dispersion curves of a surface plasmon (SP) and light in air are described by [60,61]

$$k_{SP} = \frac{\omega}{c}\sqrt{\varepsilon_m/(1+\varepsilon_m)}, \quad k_{light} = \frac{\omega}{c}, \tag{2}$$

where k_{SP} and k_{light} are the wave vectors of SP and light, ω the light frequency, c the speed of light, and ε_m the real part of the dielectric constant of gold. The dielectric constant of air is set to 1.

Figure 12 shows the dispersion curves of SP and light in air. The momentum of light is always less than that of SP for equal frequency; hence the SPP cannot be directly excited by normal incident light. Therefore, special phase-matching techniques such as grating and prime coupling were used to provide an additional wave vector Δk and ensure momentum conservation in the SPP excitation [62]. Many reports state that SPPs were efficiently excited by femtosecond laser pulses, where the additional wave vector Δk was provided by the scattered light coming from the defects fabricated in advance [32,39–41]. The SPPs cause a periodic spatial modulation of the light field, and further induce the formation of periodic ripples. In this study, the prefabricated nanogroove provides Δk when the laser polarization is perpendicular to the nanogroove, leading
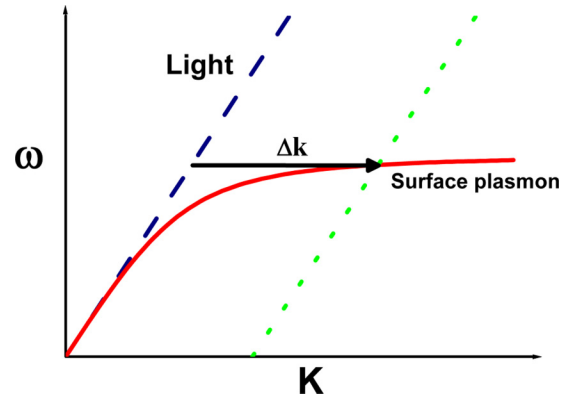
FIG. 12. Dispersion curves of SP and light in air.

to SPP excitations. With normal incident femtosecond laser pulses, the ripple period is equal to the SPP wavelength.

C. Two-temperature model

In general, the femtosecond laser ablation of a metal occurs in two stages. First, laser energy is absorbed by free electrons via the inverse Bremsstrahlung process [63,64], and deposited in the skin layer. These excited electrons reach thermal equilibrium in tens of femtoseconds via electron collisions. The electron temperature rises rapidly to over 10^4 K whereas the lattice remains at room temperature. Hot electrons cool down through two competing processes, hot-electron diffusion and electron-phonon coupling [45,64]. The transient equilibrium between the electrons and lattice takes place within tens of picoseconds through electron-phonon coupling.

The TTM is widely used to describe the electron temperature T_e and lattice temperature T_l [65,66],

$$C_e(T_e)\frac{\partial T_e}{\partial t} = \frac{\partial}{\partial x}\left[K_e(T_e,T_l)\frac{\partial T_e}{\partial x}\right] - g(T_e - T_l) + S(x,t), \tag{3}$$

$$C_l\frac{\partial T_l}{\partial t} = g(T_e - T_l), \tag{4}$$

where x is the direction perpendicular to the target surface, $C_e = A_e T_e$ and $K_e(T_e,T_l) = K_{e0}(T_e/T_l)$ are the heat capacity and thermal conductivity of electrons, $S(x,t) = \sqrt{\frac{\beta}{\pi}}\frac{(1-R)F}{t_p d}\exp[-\frac{x}{d} - \beta(\frac{t-2t_p}{t_p})^2]$ is the energy absorbed by the electron system from the laser source, $t_p = 50$ fs the laser pulse duration, d the skin depth of the laser, R the surface reflectivity, F the laser fluence, $\beta = 4\ln(2)$ the normalization factor, C_l the heat capacity of the lattice subsystem, and g the parameter associated with the electron-lattice coupling. In the initial 100 ps after laser irradiation, heat diffuses much faster through the electron subsystem, and hence the lattice thermal conductivity is neglected. Table II lists the values of the parameters in the TTM calculations obtained from [67–69].

The ultrafast evolution of the electron and lattice temperatures at the front surface of a 200-nm-thick Au film was numerically calculated by solving the TTM equations. The laser source is a 50-fs, 800-nm pulse with a fluence
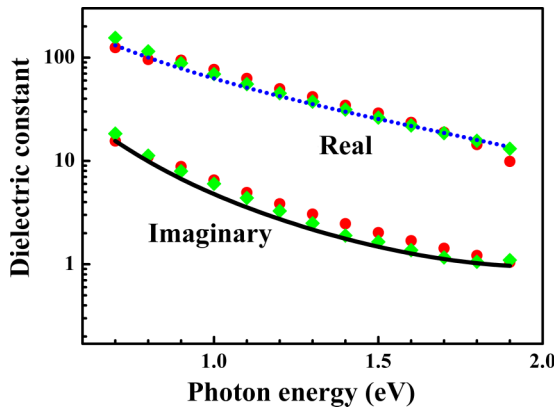

FIG. 11. Real (blue dotted curve) and imaginary (black solid curve) parts of the dielectric constant calculated from the Drude-Lorentz model. Red solid circles represent data from [57]; green solid diamonds represent data from [58].

TABLE II. Parameters used in the TTM calculations for gold film.

g (10^{16}W m^{-3} K^{-1})	A_e (J m^{-3} K^{-2})	K_{e0} (W m^{-1} K^{-1})	C_l (10^6J m^{-3} K^{-1})	T_{melt} (K)	T_{vapor} (K)	δ_s (nm)	R
2.1	71	318	2.5	1080	3150	14.4	45%

of 1.0 J/cm^2 with the peak at 50 fs [Fig. 13(a), inset]. The electron temperature increases quickly to 5.55×10^4 K after an elapsed time of 123 fs whereas the lattice temperature remains at room temperature [28,41]. Subsequently, through the electron-phonon coupling, the highly energetic electrons heat the lattice. The lattice temperature exceeds the boiling temperature of 3150 K at an elapsed time of 30 ps [Fig. 13(a)]. The surface layer vaporizes and ejects material [54,55], and the transient ripples appear tens of picoseconds later. The calculation results agree well with the experimental results (Figs. 7 and 8), where the ripples begin to appear at an elapsed time of 65 ± 20 ps for laser fluence of 1.0 J/cm^2. Figure 13(b) shows the evolution of the lattice temperature at different laser fluences. The time to reach the boiling point becomes shorter when the laser fluence increases [32], which explains well the experimental results (Fig. 8).
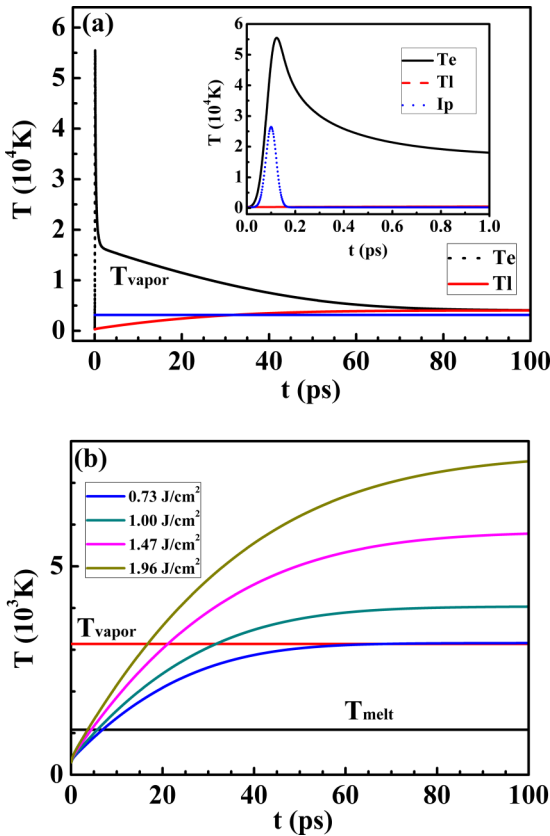
D. Electron scattering

Electron-phonon scattering and electron—electron scattering can offer free-electron momentum. They play very important roles in the electron absorption of the laser energy and the laser ablation of metal through the conservation of momentum. Gold irradiated by femtosecond laser pulses has been well studied in regard to electron-lattice nonthermal equilibrium situations [70,71]. Electron scattering involves both electron-phonon and electron-electron scattering, which are determined separately by the electron and lattice temperatures [66,71],

$$\Gamma = \Gamma_{ee} + \Gamma_{ep}, \quad \Gamma_{ee} = A_{ee}T_e^2, \quad \Gamma_{ep} = B_{ep}T_l, \quad (5)$$

where $A_{ee} = 1.2 \times 10^7$ K^{-2} s^{-1} and $B_{ep} = 1.23 \times 10^{11}$ K^{-1} s^{-1} are material constants relating to the temperature dependence of the electron-electron and electron-phonon collisional frequencies.

The calculation results obtained with the TTM indicate that the lattice temperature increases to 300–800 K in 1 ps, whereas the electron temperature is as high as $10^4 - 10^5$ K. Figure 14 shows the electron collision frequency given by Eq. (5) as a function of T_e for several values of T_l. When the electron temperature is less than 2000 K, electron collisions are mainly electron-phonon scattering. When the electron temperature is larger than 4000 K, electron-electron scattering plays the major role. The collision frequency is equal to the frequency of the 800-nm laser when the electron temperature is 5308 K. When the electron temperature is higher than 3×10^4 K, the collision frequency is greater than 10^{16} Hz [72].

The average values of the electron and lattice temperatures in the first picosecond were calculated using the TTM. The electron collision frequency as a function of laser fluence
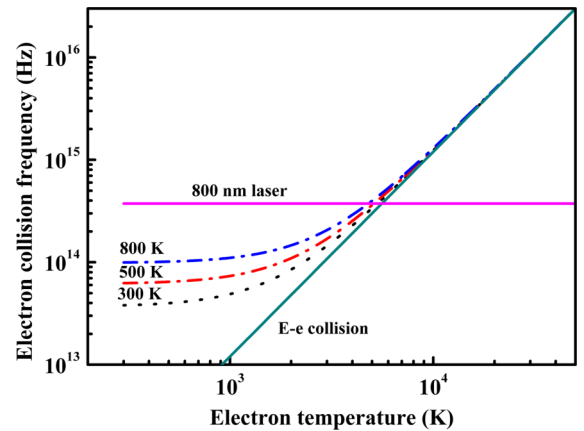

FIG. 13. (a) Time dependence of the electron and lattice temperatures at the surface of Au films irradiated by a laser pulse at a fluence of 1.0 J/cm^2. The inset shows an enlarged view in the first picosecond, where I_p is the laser intensity with peak at 100 fs. (b) Evolution of the lattice temperature for different laser fluences.

FIG. 14. Dependence of electron collision frequency on T_e and T_l. "E-e collision" shows only the electron-electron collision frequency. The total collision frequency is given for lattice temperatures at 300, 500, and 800 K.
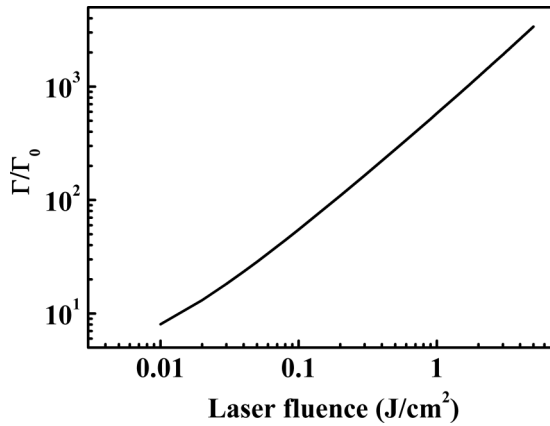
FIG. 15. Dependence of collision frequency on laser fluence.

(Fig. 15) is obtained from Eqs. (3)–(5). Figure 15 shows that the electron collision frequency increases nearly with the square of the laser fluence F; this is because the collision frequency increases with the square of the electron temperature T_e, while T_e increases linearly with F. When F increases to $2.0\,\text{J/cm}^2$, the collision frequency is enhanced by more than three orders of magnitude.

The dielectric constant of gold changes with collision frequency, as described by the modified Drude-Lorentz model. Figure 16(a) shows that the imaginary part decreases to -17.5
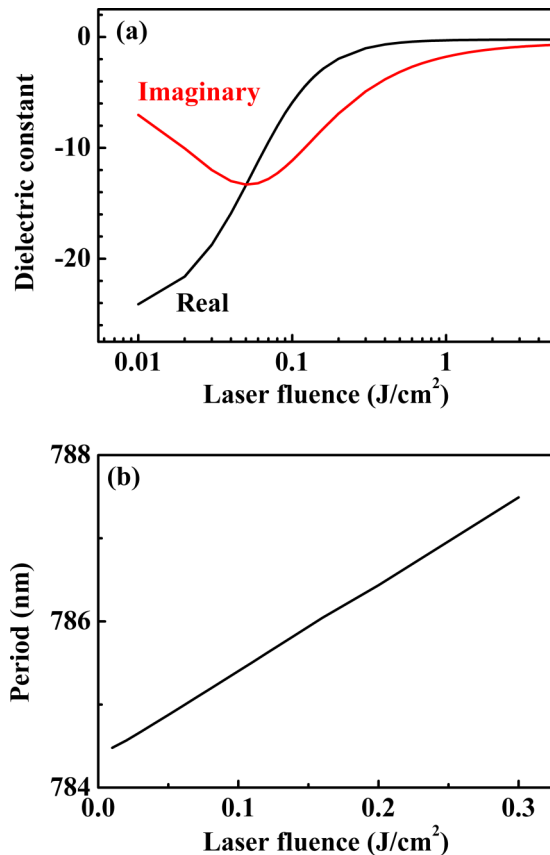

FIG. 16. Laser-fluence dependence of (a) the dielectric constant of gold and (b) the period.

as laser fluence increases to $0.5\,\text{J/cm}^2$, but then increases to -1.0 as F increases to $3.0\,\text{J/cm}^2$. The real part in contrast continuously increases with laser fluence. It is larger than -1.0 as F is larger than $0.35\,\text{J/cm}^2$, implying that SPP cannot be excited. Figure 16(b) shows that as F increases to $0.3\,\text{J/cm}^2$, the SPP wavelength and the ripple period increase from 788 to 790 nm, which is much larger than the experimental results (Fig. 9). In other words, considering only the effects of electron collision, the SPP model cannot explain the dependence of the ripple period on laser fluence.

E. Localization of hot electrons

At room temperature, the electron collision frequency of gold is mainly determined by electron-phonon scattering. It is less than that of the 800-nm light and the electrons can synchronously oscillate with the laser field.

The electron-electron collision frequency increases with the square of electron temperature. Figure 14 shows that the electron collision frequency is 10^{16} Hz as electron temperature is 3×10^4 K. Assuming a Boltzmann distribution, the average kinetic energy and velocity are 4.14×10^{-19} J and 0.95 nm/fs, respectively. In successive collisions, an electron moves only 0.095 nm on average, implying that the electrons are bound and cannot synchronously oscillate with the laser field. In this case, the very hot electrons become bound electrons.

When the electron temperature is 5308 K, the electron collision frequency is equal to the frequency of the 800-nm light. We propose here that when the collision frequency is larger than the laser frequency, the electrons cannot effectively take part in the collective oscillation of the surface plasmon and are not sufficiently free electrons.

The velocity distributions of electrons at different temperatures follow Boltzmann's distribution (Fig. 17). With the above analysis, we propose that the electron can effectively participate in the collective oscillation when the collision frequency is less than the frequency of the 800-nm light; namely, the electrons in the yellow region are free electrons, whereas the others are bound. Therefore, the numerical density of effective free electrons decreases with increasing electron temperature.
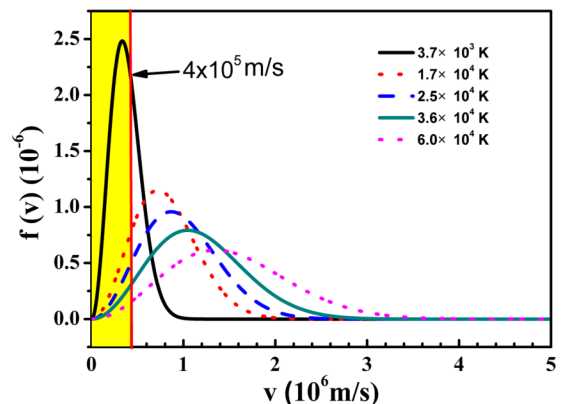

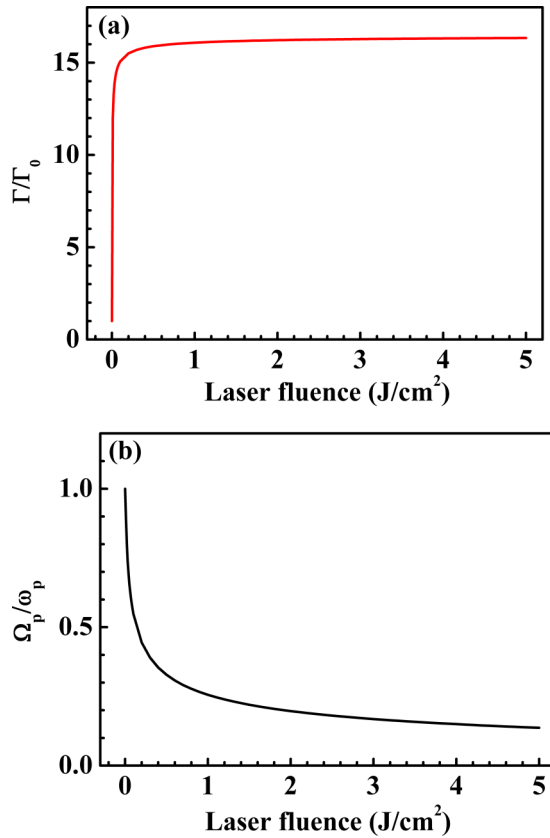FIG. 17. Velocity distributions at different electron temperatures.

FIG. 18. Laser-fluence dependence of (a) the collision frequency of effective free electrons, and (b) the resonant frequency, where Γ_0 is the electron collision frequency and ω_p is the resonance frequency of plasma at room temperature.

The average temperature of electrons in the first picosecond is calculated using the TTM for different laser fluences. The laser-fluence dependence of the collision frequency for effective free electrons [Fig. 18(a)] shows that for $F > 0.05 \, \mathrm{J/cm^2}$, the collision frequency of effective free electrons increases quickly by a factor of 14. With F further increases, Γ/Γ_0 increases slowly to 16.3, a limit value equal to the 800-nm light frequency.

The resonance frequency of plasma is proportional to the square root of the electron numerical density. The effective free-electron density and the resonance frequency of the surface plasmon decrease rapidly with laser fluence [Fig. 18(b)]. The resonant frequency Ω_p is less than 0.4 times the initial value of ω_p if F is $0.3 \, \mathrm{J/cm^2}$; then it decreases slowly to 0.15 when the laser fluence increases to $4.0 \, \mathrm{J/cm^2}$.

The dielectric constant changes with the collision frequency of electrons and the resonance frequency of plasma, as described by the modified version of the Drude-Lorentz model. The imaginary part decreases to -7.9 as laser fluence increases to $0.006 \, \mathrm{J/cm^2}$, then increases to -1.0 as F increases to $1.6 \, \mathrm{J/cm^2}$ [Fig. 19(a)]. The real part increases with laser fluence. It is larger than -1.0 as F is larger than $1.9 \, \mathrm{J/cm^2}$. Figure 19(b) shows that as F increases to $1.9 \, \mathrm{J/cm^2}$, the SPP wavelength and the ripple period decrease from 784 to 606 nm, which opposes the trend found in experimental results for which the period increases from 685
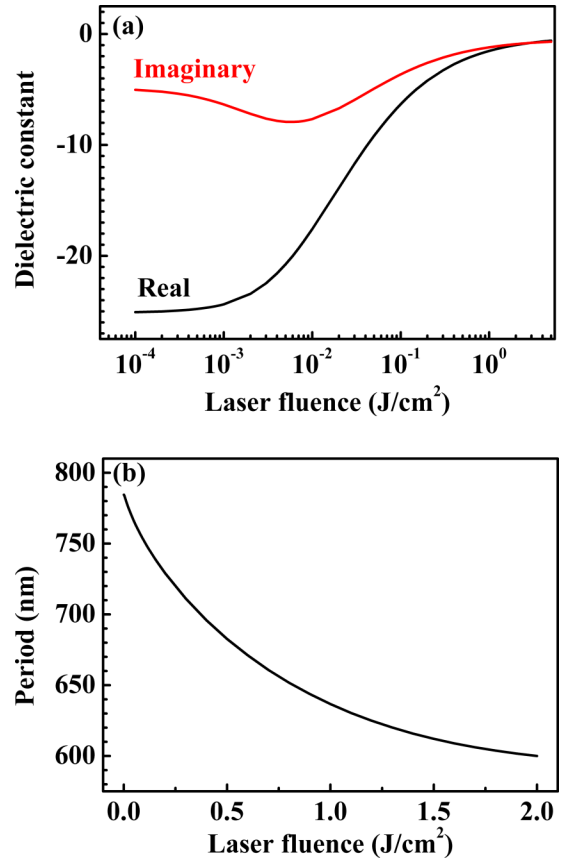

FIG. 19. Laser-fluence dependence of (a) the dielectric constant and (b) the ripple period.

to 770 nm as F increases from 0.73 to $3.42 \, \mathrm{J/cm^2}$ (Fig. 9). Therefore, the ripple period predicted using the SPP model and considering only the effects of electron collision and localization is within the range of experimental results, but the trends are contrary.

F. Transition of *d*-band electrons

The dielectric constant of gold includes contributions from the excitation of free electrons and the interband absorption [56–58]. The absorption of *d*-band electrons influences the optical properties of gold, silver, and copper [37,38,73]. However, most studies on the dynamics of laser ablation usually focus on changes in optical properties arising from electron-electron scattering and electron-phonon scattering along with changes in the electron and lattice temperatures. The contribution of the *d*-band transition to the dielectric constant is treated as constant, even for excitations by an intense femtosecond laser pulse. Clearly, the issue is worth an in-depth study.

Interband and intraband contributions in the femtosecond laser ablation in copper and aluminum were studied using a comparative investigation of the experimental and simulated transient optical properties [37,72]. The results indicated that interband rather than intraband absorption is the major contributor to laser absorption that increases the transient dielectric constant steeply. Even during femtosecond laser ablation of transparent materials, interband absorption also plays a very important role [74].
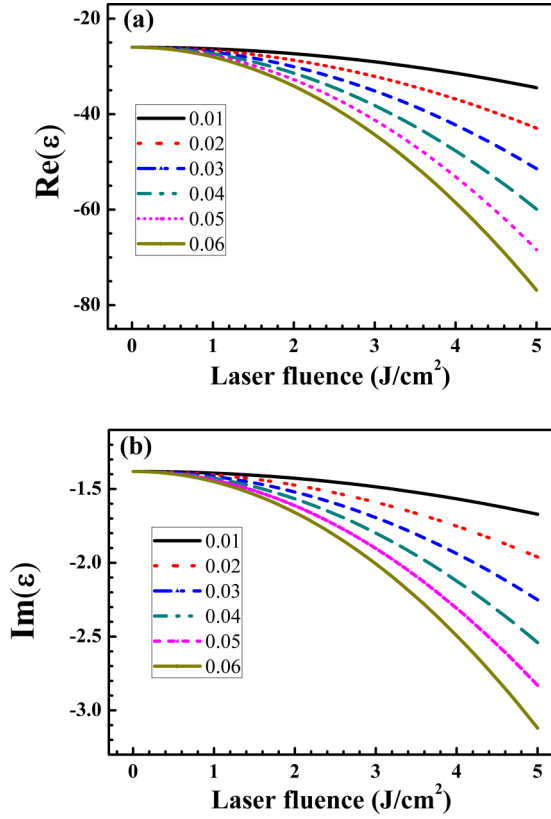
FIG. 21. Ripple period as a function of laser fluence F for various values of parameter x.

calculated using the SPP model based on the results in Fig. 20, increases with laser fluence and parameter x, the trends being similar to the experimental results (Fig. 9) although the values are much larger.

G. Dielectric constant of the excited state and ripple period

The plasma resonance frequency Ω_p, the electron collision frequency Γ, and the transition of d-band electrons all change with laser fluence F. Therefore, the dielectric constant of the

FIG. 20. (a) Real and (b) imaginary parts of the dielectric constant as a function of laser fluence F for various values of parameter x.

In noble metals such as silver and gold, d-band absorption plays an important role, especially when the laser fluence rises above the melting and ablation threshold [38,73]. Chan *et al.* reported the absorption of a femtosecond laser in Ag film. The absorbed energy increases nonlinearly when the laser fluence is larger than half the melting threshold. They proposed that nonlinear absorptions were caused by the excitation of the d-band electrons below the Fermi surface [38]. The photon energy of an 800-nm laser pulse is 1.55 eV, which is less than the d-band level of -1.84 eV [75]. Therefore, the d-band electron transition in gold is a two-photon process.

According to the above discussions, electrons in the d band are excited via two-photon absorption and becoming free. Hence it contributes to the second term in Eq. (3) via a factor xF^2, x being a parameter related to the two-photon absorption coefficient. The dielectric constant with only d-band transitions contributing is written

$$\varepsilon = 1 - \frac{f_0(\omega_p)^2 + xF^2(\omega_p)^2}{\omega(\omega - i\Gamma_0)} + \sum_{j=1}^{3} \frac{f_j(\omega_p)^2}{\omega_j^2 - \omega^2 + i\omega\Gamma_j}. \quad (6)$$

From the laser-fluence dependence of the real and imaginary parts of the dielectric constant [Figs. 20(a) and 20(b)], both decrease with F because of the term $xF^2(\omega_p)^2$. Moreover, the dielectric constant decreases more quickly with larger x values. When $F = 2.0\,\mathrm{J/cm^2}$, the real/imaginary part decreases to $-27.4/-1.43$ for $x = 0.01$, whereas they are $-34.1/-1.66$ for $x = 0.06$. The ripple period (Fig. 21),
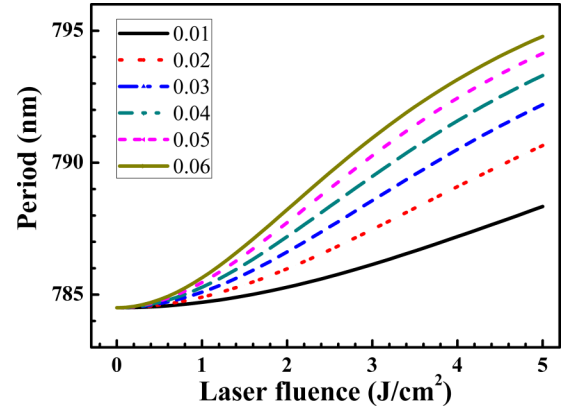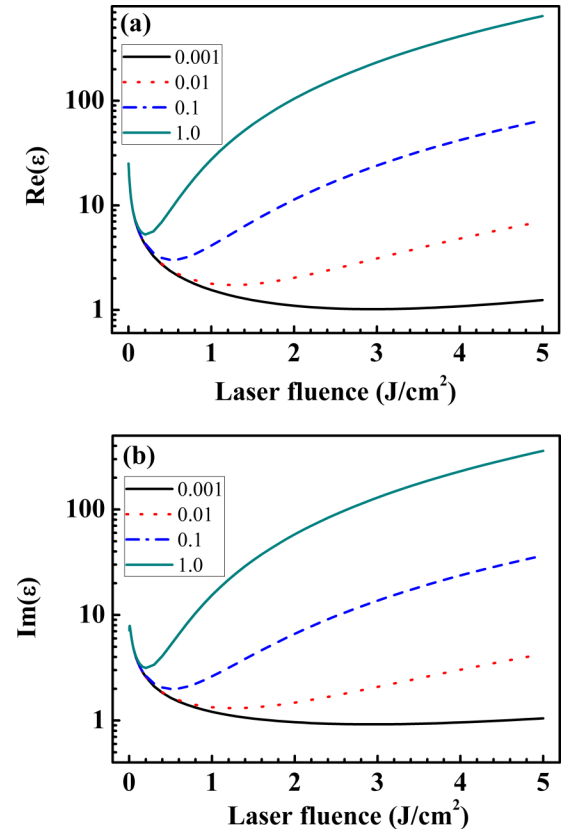

FIG. 22. (a) Real and (b) imaginary parts of the dielectric constant as a function of laser fluence F for various values of parameter x.
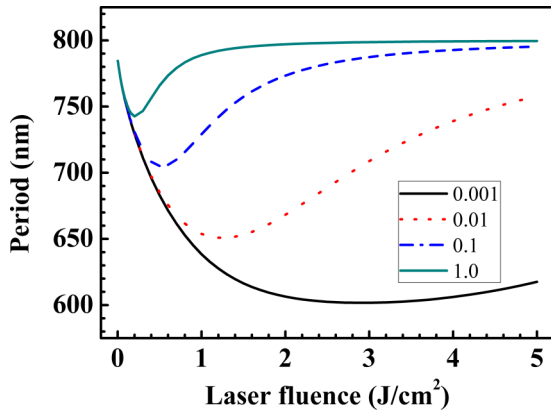
FIG. 23. Ripple period as a function of laser fluence *F* for various values of parameter *x*.

excited state is expressible as

$$\varepsilon = 1 - \frac{f_0[\Omega_p(F)]^2 + xF^2(\omega_p)^2}{\omega[\omega - i\Gamma(F)]} + \sum_{j=1}^{3} \frac{f_j(\omega_p)^2}{\omega_j^2 - \omega^2 + i\omega\Gamma_j}. \tag{7}$$

Using our numerical results (Figs. 18–20), we calculated the dependence of the dielectric constant on laser fluence *F* for different values of parameter *x*. As *F* increases to 0.2 J/cm^2, the real part of the dielectric constant [Fig. 22(a)] increases to −4.2 to −5.3 for *x* in the range 0.001–1.0 because both hot-electron localization and collision frequency are enhanced with laser fluence. However, with a further increase in laser fluence, they vary greatly with parameter *x*. The effect from *d*-band transitions is small for *x* = 0.001, and the real part increases slowly with *F*. The *d*-band transition dominates the real part for *x* = 1.0. It decreases from −5.65 to −105 as *F* increases from 0.3 to 2.0 J/cm^2. The imaginary part [Fig. 22(b)] has a similar trend as the real part, and therefore is not discussed further.

The ripple periods obtained from the SPP model (Fig. 23) show that results for *x* = 0.001 are similar when only the effects of hot-electron localization [Fig. 19(b)] are taken into account because the *d*-band electron transitions are weak. The period decreases to 593 nm with laser fluences up to
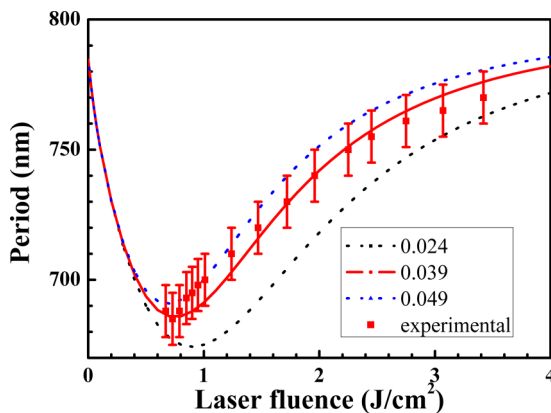
F = 1.2 J/cm^2 but subsequently increases slowly. If *x* is set to 1.0, the period decreases quickly for *F* < 0.2 J/cm^2, and then increases to 795 nm up to *F* = 1.6 J/cm^2. Clearly, for *x* = 0.1, this laser-fluence dependence of the period is consistent with the experimental trend. With a precise adjustment of *x*, the value *x* = 0.039 reproduces well the experiment results (Fig. 24). For *x* = 0.024 and 0.049, the periods are close to the lower and upper limits, respectively, given by the experimental error.

V. CONCLUSIONS

In summary, the dynamics of ripple formation on the surface of gold film induced by a single 800-nm, 50-fs laser pulse were investigated by the collinear pump-probe imaging method. A nanogroove with a width of 400 nm and depth of 20 nm was etched by femtosecond laser direct writing prior to experiments. With the laser polarization perpendicular to the nanogroove, transient ripples appeared after an elapsed time of 25–100 ps, and they became regular and clear after 400–600 ps, depending on laser fluence. The ripple period increased from 685 to 770 nm with increasing fluence from 0.73 to 3.42 J/cm^2. However, with the laser polarization parallel to the nanogroove, no transient ripples were observed during the entire ablation process, because the conservation of momentum cannot be satisfied and SPP cannot be excited. These results indicate that SPP excitation plays a critical role in the formation of the ripples. However, the period observed in experiments is much shorter than the value obtained from the SPP model assuming a dielectric constant of gold for the ground state. In order to further understand the ultrafast dynamics during the formation of periodic ripples and the disparity of ripple periods between SPP model and experiments, we made the following theoretical study.

The evolution of both the electron and lattice temperatures is theoretically studied using the TTM. The electron temperature rose to several 10^4 K in 50 fs after laser irradiation with fluences of 0.7−5.0 J/cm^2. The collision frequency of these hot electrons increased above the frequency of the 800-nm laser. Therefore, they are unable to oscillate synchronously with the laser field and cannot participate in the SPP excitation. Their localization decreases the numerical density of free electrons and plasma frequency, which further reduces the period for higher laser fluences. Moreover, the *d*-band electrons in gold can be excited to energy levels above the Fermi surface through two-photon absorption under laser irradiation becoming free electrons. The plasma frequency and dielectric constant of the excited states are modified by a factor xF^2, with the period then increasing with laser fluence because of the *d*-band transitions. Given the dielectric constant for excited states, including the effects of hot-electron localization and *d*-band transitions, the ripple period obtained from the SPP model with *x* set to 0.039 decreases to 685 nm as laser fluence increases up to 0.75 J/cm^2 and increases to 756 nm as *F* increases to 2.5 J/cm^2. The theoretical values agree well with the experimental results, which supports the view that the SPP excitations play a very important role in the formation of periodic ripples in metal surfaces induced by femtosecond laser pulses.

FIG. 24. Dependence of ripple period on laser fluence *F*. Red squares and error bars are experimental data.

[1] M. Birnbaum, Semiconductor surface damage produced by ruby lasers, J. Appl. Phys. **36**, 3688 (1965).

[2] D. C. Emmony, R. P. Howson, and L. J. Willis, Laser mirror damage in germanium at 10.6 μm, Appl. Phys. Lett. **23**, 598 (1973).

[3] J. E. Sipe, J. F. Young, J. S. Preston, and H. M. Van Driel, Laser-induced periodic surface structure. I. Theory, Phys. Rev. B **27**, 1141 (1983).

[4] Y. Shimotsuma, P. G. Kazansky, J. Qiu, and K. Hirao, Self-Organized Nanogratings in Glass Irradiated by Ultrashort Light Pulses, Phys. Rev. Lett. **91**, 247405 (2003).

[5] N. Yasumaru, K. Miyazaki, and J. Kiuchi, Femtosecond-laser-induced nanostructure formed on hard thin films of TiN and DLC, Appl. Phys. A **76**, 983 (2003).

[6] T. Q. Jia, H. X. Chen, M. Huang, F. L. Zhao, J. R. Qiu, R. X. Li, Z. Z. Xu, X. K. He, J. Zhang, and H. Kuroda, Formation of nanogratings on the surface of a ZnSe crystal irradiated by femtosecond laser pulses, Phys. Rev. B **72**, 125429 (2005).

[7] J. Wang and C. Guo, Ultrafast dynamics of femtosecond laser-induced periodic surface pattern formation on metals, Appl. Phys. Lett. **87**, 251914 (2005).

[8] G. Miyaji and K. Miyazaki, Ultrafast dynamics of periodic nanostructure formation on diamondlike carbon films irradiated with femtosecond laser pulses, Appl. Phys. Lett. **89**, 191902 (2006).

[9] J. Bonse, A. Rosenfeld, and J. Krüger, On the role of surface plasmon polaritons in the formation of laser-induced periodic surface structures upon irradiation of silicon by femtosecond-laser pulses, J. Appl. Phys. **106**, 104910 (2009).

[10] M. Huang, F. Zhao, Y. Cheng, N. Xu, and Z. Xu, Origin of laser-induced near-subwavelength ripples: Interference between surface plasmons and incident laser, ACS Nano **3**, 4062 (2009).

[11] K. Okamuro, M. Hashida, Y. Miyasaka, Y. Ikuta, S. Tokita, and S. Sakab, Laser fluence dependence of periodic grating structures formed on metal surfaces under femtosecond laser pulse irradiation, Phys. Rev. B **82**, 165417 (2010).

[12] A. Y. Vorobyev, V. S. Makin, and C. Guo, Brighter Light Sources from Black Metal: Significant Increase in Emission Efficiency of Incandescent Light Sources, Phys. Rev. Lett. **102**, 234301 (2009).

[13] A. Y. Vorobyev and C. Guo, Direct femtosecond laser surface nano/microstructuring and its applications, Laser Photonics Rev. **7**, 385 (2013).

[14] X. Jia, T. Jia, Yi Zhang, P. Xiong, D. Feng, Z. Sun, and Z. Xu, Optical absorption of two dimensional periodic microstructures on ZnO crystal fabricated by the interference of two femtosecond laser beams, Opt. Express **18**, 14401 (2010).

[15] P. Xiong, T. Jia, X. Jia, D. Feng, S. Zhang, L. Ding, Z. Sun, J. Qiu, and Z. Xu, Ultraviolet luminescence enhancement of ZnO two-dimensional periodic nanostructures fabricated by the interference of three femtosecond laser beams, New J. Phys. **13**, 023044 (2011).

[16] J. Pan, T. Jia, X. Jia, D. Feng, S. Zhang, Z. Sun, and J. Qiu, Infrared femtosecond laser-induced great enhancement of ultraviolet luminescence of ZnO two-dimensional nanostructures, Appl. Phys. A **117**, 1923 (2014).

[17] J. Pan, T. Jia, Y. Huo, X. Jia, D. Feng, S. Zhang, Z. Sun, and Z. Xu, Great enhancement of near band-edge emission of ZnSe two-dimensional complex nanostructures fabricated by the interference of three femtosecond laser beams, J. Appl. Phys. **114**, 093102 (2013).

[18] A. Y. Vorobyev and C. Guo, Colorizing metals with femtosecond laser pulses, Appl. Phys. Lett. **92**, 041914 (2008).

[19] B. Dusser, Z. Sagan, H. Soder, N. Faure, J. P. Colombier, M. Jourlin, and E. Audouard, Controlled nanostructrures formation by ultra fast laser pulses for color marking, Opt. Express **18**, 2913 (2010).

[20] H. Pan, F. Luo, G. Lin, C. Wang, M. Dong, Y. Liao, and Q.-Z. Zhao, Quasi-superhydrophobic porous silicon surface fabricated by ultrashort pulsed-laser ablation and chemical etching, Chem. Phys. Lett. **637**, 159 (2015).

[21] H.-J. Li, W.-Z. Fan, H.-H. Pan, C.-W. Wang, J. Qian, and Q.-Z. Zhao, Fabrication of "petal effect" surfaces by femtosecond laser-induced forward transfer, Chem. Phys. Lett. **667**, 20 (2017).

[22] A. Y. Vorobyev and C. Guo, Multifunctional surfaces produced by femtosecond laser pulses, J. Appl. Phys. **117**, 033103 (2015).

[23] W. He, J. Yang, and C. Guo, Controlling periodic ripple microstructure formation on 4H-SiC crystal with three time-delayed femtosecond laser beams of different linear polarizations, Opt. Express **25**, 5156 (2017).

[24] J. Reif, O. Varlamova, and F. Costache, Femtosecond laser induced nanostructure formation: Self-organization control parameters, Appl. Phys. A **92**, 1019 (2008).

[25] J. Reif, O. Varlamova, S. Uhlig, S. Varlamov, and M. Bestehorn, On the physics of self-organized nanostructure formation upon femtosecond laser ablation, Appl. Phys. A **117**, 179 (2014).

[26] E. L. Gurevich, Self-organized nanopatterns in thin layers of superheated liquid metals, Phys. Rev. E **83**, 031604 (2011).

[27] F. Garrelie, J. P. Colombier, F. Pigeon, S. Tonchev, N. Faure, M. Bounhalli, S. Reynaud, and O. Parriaux, Evidence of surface plasmon resonance in ultrafast laser-induced ripples, Opt. Express **19**, 9035 (2011).

[28] K. Zhou, X. Jia, T. Jia, K. Cheng, K. Cao, S. Zhang, D. Feng, and Z. Sun, The influences of surface plasmons and thermal effects on femtosecond laser-induced subwavelength periodic ripples on Au film by pump-probe imaging, J. Appl. Phys. **121**, 104301 (2017).

[29] Y. Dong, and P. Molian, Coulomb explosion-induced formation of highly oriented nanoparticles on thin films of 3C–SiC by the femtosecond pulsed laser, Appl. Phys. Lett. **84**, 10 (2004).

[30] S. Kumar Das, H. Messaoudi, A. Debroy, E. McGlynn, and R. Grunwald, Multiphoton excitation of surface

plasmon-polaritons and scaling of nanoripple formation in large bandgap materials, Opt. Mater. Express **3**, 1705 (2013).

[31] J. Liu, T. Jia, H. Zhao, and Y. Huang, Two-photon excitation of surface plasmon and the period-increasing effect of low spatial frequency ripples on a GaP crystal in air/water, J. Phys. D: Appl. Phys. **49**, 435105 (2016).

[32] J. Liu, X. Jia, W. Wu, K. Cheng, D. Feng, S. Zhang, Z. Sun, and T. Jia, Ultrafast imaging on the formation of periodic ripples on a Si surface with a prefabricated nanogroove induced by a single femtosecond laser pulse, Opt. Express **26**, 6302 (2018).

[33] M. Hashida, Y. Miyasaka, Y. Ikuta, S. Tokita, and S. Sakabe, Crystal structures on a copper thin film with a surface of periodic self-organized nanostructures induced by femtosecond laser pulses, Phys. Rev. B **83**, 235413 (2011).

[34] S. Bashir, M. S. Rafique, C. S. Nathala, A. A. Ajami, and W. Husinsky, Femtosecond laser fluence based nanostructuring of W and Mo in ethanol, Physica B (Amsterdam, Neth.) **513**, 48 (2017).

[35] S. Sakabe, M. Hashida, S. Tokita, S. Namba, and K. Okamuro, Mechanism for self-formation of periodic grating structures on a metal surface by a femtosecond laser pulse, Phys. Rev. B **79**, 033409 (2009).

[36] E. V. Golosov, A. A. Ionin, Yu. R. Kolobov, S. I. Kudryashov, A. E. Ligachev, S. V. Makarov, Yu. N. Novoselov, L. V. Seleznev, and D. V. Sinitsyn, Formation of periodic nanostructures on aluminum surface by femtosecond laser pulses, Nanotechnol. Russ. **6**, 237 (2011).

[37] J. Winter, S. Rapp, M. Schmidt, and H. P. Huber, Ultrafast laser processing of copper: A comparative study of experimental and simulated transient optical properties, Appl. Surf. Sci. **417**, 2 (2017).

[38] W.-L. Chan, R. S. Averback, and D. G. Cahill, Nonlinear energy absorption of femtosecond laser pulses in noble metals, Appl. Phys. A **97**, 287 (2009).

[39] R. D. Murphy, B. Torralva, D. P. Adams, and S. M. Yalisove, Laser-induced periodic surface structure formation resulting from single-pulse ultrafast irradiation of Au microstructures on a Si substrate, Appl. Phys. Lett. **102**, 211101 (2013).

[40] R. D. Murphy, B. Torralva, D. P. Adams, and S. M. Yalisove, Polarization dependent formation of femtosecond laser-induced periodic surface structures near stepped features, Appl. Phys. Lett. **104**, 231117 (2014).

[41] M. Yang, Q. Wu, Z. Chen, B. Zhang, B. Tang, J. Yao, I. Drevensek-Olenik, and J. Xu, Generation and erasure of femtosecond laser-induced periodic surface structures on nanoparticle-covered silicon by a single laser pulse, Opt. Lett. **39**, 343 (2014).

[42] R. D. Murphy, B. Torralva, D. P. Adams, and S. M. Yalisove, Pump-probe imaging of laser-induced periodic surface structures after ultrafast irradiation of Si, Appl. Phys. Lett. **103**, 141104 (2013).

[43] K. R. P. Kafka, D. R. Austin, H. Li, A. Y. Yi, J. Cheng, and E. A. Chowdhury, Time-resolved measurement of single pulse femtosecond laser-induced periodic surface structure formation induced by a pre-fabricated surface groove, Opt. Express **23**, 19432 (2015).

[44] X. Jia, T. Q. Jia, N. N. Peng, D. H. Feng, S. A. Zhang, and Z. R. Sun, Dynamics of femtosecond laser-induced periodic surface structures on silicon by high spatial and temporal resolution imaging, J. Appl. Phys. **115**, 143102 (2014).

[45] J. Wang and C. Guo, Numerical study of ultrafast dynamics of femtosecond laser-induced periodic surface structure formation on noble metals, J. Appl. Phys. **102**, 053522 (2007).

[46] A. Y. Vorobyev, V. S. Makin, and C. Guo, Periodic ordering of random surface nanostructures induced by femtosecond laser pulses on metals, J. Appl. Phys. **101**, 034903 (2007).

[47] X. Jia, T. Q. Jia, Y. Zhang, P. X. Xiong, D. H. Feng, Z. R. Sun, J. R. Qiu, and Z. Z. Xu, Periodic nanoripples in the surface and subsurface layers in ZnO irradiated by femtosecond laser pulses, Opt. Lett. **35**, 1248 (2010).

[48] Y. Huo, T. Jia, D. Feng, S. Zhang, J. Liu, J. Pan, K. Zhou, and Z. Sun, Formation of high spatial frequency ripples in stainless steel irradiated by femtosecond laser pulses in water, Laser Phys. **23**, 056101 (2013).

[49] K. Zhou, X. Jia, H. Xi, J. Liu, D. Feng, S. Zhang, Z. Sun, and T. Jia, Periodic surface structures on Ni–Fe film induced by a single femtosecond laser pulse with diffraction rings, Chin. Opt. Lett. **15**, 022201 (2017).

[50] F. Korte, J. Koch, and B. N. Chichkov, Formation of microbumps and nanojets on gold targets by femtosecond laser pulses, Appl. Phys. A **79**, 879 (2004).

[51] J. Bonse and J. Krüger, Pulse number dependence of laser-induced periodic surface structures for femtosecond laser irradiation of silicon, J. Appl. Phys. **108**, 034903 (2010).

[52] G. D. Tsibidis, M. Barberoglou, P. A. Loukakos, E. Stratakis, and C. Fotakis, Dynamics of ripple formation on silicon surfaces by ultrashort laser pulses in subablation conditions, Phys. Rev. B **86**, 115316 (2012).

[53] S. L. Daraszewicz, Y. Giret, N. Naruse, Y. Murooka, J. Yang, D. M. Duffy, A. L. Shluger, and K. Tanimura, Structural dynamics of laser-irradiated gold nanofilms, Phys. Rev. B **88**, 184101 (2013).

[54] N. Zhang, X. Zhu, J. Yang, X. Wang, and M. Wang, Time-Resolved Shadowgraphs of Material Ejection in Intense Femtosecond Laser Ablation of Aluminum, Phys. Rev. Lett. **99**, 167602 (2007).

[55] Z. Wu, X. Zhu, and N. Zhang, Time-resolved shadowgraphic study of femtosecond laser ablation of aluminum under different ambient air pressures, J. Appl. Phys. **109**, 053113 (2011).

[56] A. D. Rakić, A. B. Djurišić, J. M. Elazar, and M. L. Majewski, Optical properties of metallic films for vertical-cavity optoelectronic devices, Appl. Opt. **37**, 5271 (1998).

[57] D. W. Lynch and W. R. Hunter, *Handbook of Optical Constants of Solids*, edited by E. D. Palik (Academic Press, New York, 1985).

[58] P. B. Johnson and R. W. Christy, Optical constants of the noble metals, Phys. Rev. B **6**, 4370 (1972).

[59] I. Gnilitskyi, T. J.-Y. Derrien, Y. Levy, N. M. Bulgakova, T. Mocek, and L. Orazi, High-speed manufacturing of highly regular femtosecond laser-induced periodic surface structures: Physical origin of regularity, Sci. Rep. **7**, 8485 (2017).

[60] H. Raether, *Surface Plasmons on Smooth and Rough Surfaces and on Gratings* (Springer-Verlag, Berlin, 1988).

[61] E. L. Gurevich and S. V. Gurevich, Laser induced periodic surface structures induced by surface plasmons coupled via roughness, Appl. Surf. Sci. **302**, 118 (2014).

[62] S. A. Maier, *Plasmonics: Fundamentals and Applications* (Springer, New York, 2007).

[63] S. Nolte, C. Momma, H. Jacobs, A. Tünnermann, B. N. Chichkov, B. Wellegehausen, and H. Welling, Ablation of

metals by ultrashort laser pulses, J. Opt. Soc. Am. B **14**, 2716 (1997).

[64] B. N. Chichkov, C. Momma, S. Nolte, F. Von Alvensleben, and A. Tünnermann, Femtosecond, picosecond and nanosecond laser ablation of solids, Appl. Phys. A **63**, 109 (1996).

[65] S. I. Anisimov, B. L. Kapeliovich, and T. L. Perel'man, Electron emission from metal surfaces exposed to ultrashort laser pulses, Sov. Phys. JETP **39**, 375 (1974).

[66] P. E. Hopkins, J. L. Kassebaum, and P. M. Norris, Effects of electron scattering at metal-nonmetal interfaces on electron-phonon equilibration in gold films, J. Appl. Phys. **105**, 023710 (2009).

[67] Y. P. Meshcheryakov and N. M. Bulgakova, Thermoelastic modeling of microbump and nanojet formation on nanosize gold films under femtosecond laser irradiation, Appl. Phys. A **82**, 363 (2006).

[68] M. Bonn, D. N. Denzler, S. Funk, M. Wolf, S.-S. Wellershoff, and J. Hohlfeld, Ultrafast electron dynamics at metal surfaces: Competition between electron-phonon coupling and hot-electron transport, Phys. Rev. B **61**, 1101 (2000).

[69] A. Y. Vorobyev and C. Guo, Direct observation of enhanced residual thermal energy coupling to solids in femtosecond laser ablation, Appl. Phys. Lett. **86**, 011916 (2005).

[70] J. Hohlfeld, S.-S. Wellershoff, J. Gudde, U. Conrad, V. Jahnke, and E. Matthias, Electron and lattice dynamics following optical excitation of metals, Chem. Phys. **251**, 237 (2000).

[71] X. Y. Wang, D. M. Riffe, Y.-S. Lee, and M. C. Downer, Time-resolved electron-temperature measurement in a highly excited gold target using femtosecond thermionic emission, Phys. Rev. B **50**, 8016 (1994).

[72] D. Fisher, M. Fraenkel, Z. Henis, E. Moshe, and S. Eliezer, Interband and intraband (Drude) contributions to femtosecond laser absorption in aluminum, Phys. Rev. E **65**, 016409 (2001).

[73] B. Y. Mueller and B. Rethfeld, Relaxation dynamics in laser-excited metals under nonequilibrium conditions, Phys. Rev. B **87**, 035139 (2013).

[74] T. Q. Jia, H. X. Chen, M. Huang, F. L. Zhao, X. X. Li, S. Z. Xu, H. Y. Sun, D. H. Feng, C. B. Li, X. F. Wang, R. X. Li, Z. Z. Xu, X. K. He, and H. Kuroda, Ultraviolet-infrared femtosecond laser-induced damage in fused silica and CaF^2 crystals, Phys. Rev. B **73**, 054105 (2006).

[75] L. Le Thi Ngoc, J. Wiedemair, A. van denBerg, and E. T. Carlen, Plasmon-modulated photoluminescence from gold nanostructures and its dependence on plasmon resonance, excitation energy, and band structure, Opt. Express **23**, 5547 (2015).